Synthesis of Doubly-Connected Metamaterial Coatings within the Material-by-Design Paradigm

M. Salucci, A. Polo, and G. Oliveri

Abstract

In this work, an innovative transformation electromagnetics (*TE*) method is proposed to design metamaterial lenses with doubly-connected contours. Such field manipulation devices (*FMD*s) can be exploited to effectively design high-performance conformal phased arrays installed on masts of arbitrarily-shaped sections. Towards this aim, the design problem is formulated within the Material-by-Design (*MbD*) paradigm and it is effectively solved thanks to an innovative *TE* methodology based on the Schwarz-Christoffel (*SC*) transformation theorem. Some numerical results are provided in order to verify the effectiveness of the proposed *MbD SC-TE* technique.

1 Definitions

- Maximum directivity

$$D_{max}(\theta, \varphi) = \frac{4\pi \max_{(\theta,\varphi)}\{|E(\theta,\varphi)|^2\}}{\int_0^{2\pi}\int_0^{\pi} |E(\theta,\varphi)|^2 \sin(\theta) d\theta d\varphi} \tag{1}$$

- Sidelobe level (SLL)

$$SLL = 20 \times log_{10}\left(\frac{\max\{F(\theta,\varphi)\}}{\max\{E(\theta,\varphi)\}}\right) \tag{2}$$

where $F(\theta, \varphi)$ is the $E(\theta, \varphi)$ secondary lobes

- Maximum lens permittivity

$$\max\{\underline{\underline{\varepsilon}}\} = \max_{\underline{r}\in\Omega}\{\varepsilon_{pq}(\underline{r});\, p, q\, \in \{1, 2, 3\}\} \tag{3}$$

- Minimum lens permittivity

$$\min\{\underline{\underline{\varepsilon}}\} = \min_{\underline{r}\in\Omega}\{\varepsilon_{pq}(\underline{r});\, p, q\, \in \{1, 2, 3\}\} \tag{4}$$

- Average fractional anisotropy

$$\alpha_F = \frac{1}{area(\Omega)} \int_{\underline{r}\in\Omega} \sqrt{\frac{3\sum_{i=1}^{3}[\sigma_i(\underline{r}) - \sigma_{ave}(\underline{r})]^2}{2\sum_{i=1}^{3}[\sigma_i(\underline{r})]^2}} d\underline{r} \tag{5}$$

- Average relative anisotropy

$$\alpha_R = \frac{1}{area(\Omega)} \int_{\underline{r}\in\Omega} \sqrt{\frac{\sum_{i=1}^{3}[\sigma_i(\underline{r}) - \sigma_{ave}(\underline{r})]^2}{3\sigma_{ave}(\underline{r})}} d\underline{r} \tag{6}$$

where

  - $\sigma_i(\underline{r}),\ i = 1, ..., 3$ are the eigenvalues of the permittivity tensor $\underline{\underline{\varepsilon}}(\underline{r})$;
  - $\sigma_{ave}(\underline{r}) = \frac{\sum_{i=1}^{3}\sigma_i(\underline{r})}{3}$ is the average of the eigenvalues;
  - Ω is the space region that defines the lens

- Far-Field Matching Error

$$\xi = \frac{\sum_{u=1}^{U}\sum_{v=1,\ (u,v)\notin\Omega}^{V} |E_{est}(\theta_u, \varphi_v) - E_{ref}(\theta_u, \varphi_v)|^2}{\sum_{u=1}^{U}\sum_{v=1,\ (u,v)\notin\Omega}^{V} |E_{ref}(\theta_u, \varphi_v)|^2} \tag{7}$$

- Near-Field Matching Error

$$\chi = \frac{\sum_{u=1}^{U}\sum_{v=1,\ (u,v)\notin\Omega}^{V} |E_{est}(x_u, y_v) - E_{ref}(x_u, y_v)|^2}{\sum_{u=1}^{U}\sum_{v=1,\ (u,v)\notin\Omega}^{V} |E_{ref}(x_u, y_v)|^2} \tag{8}$$

2 Numerical Assessment

2.1 Analysis Vs. the Number of Elements

2.1.1 Parameters

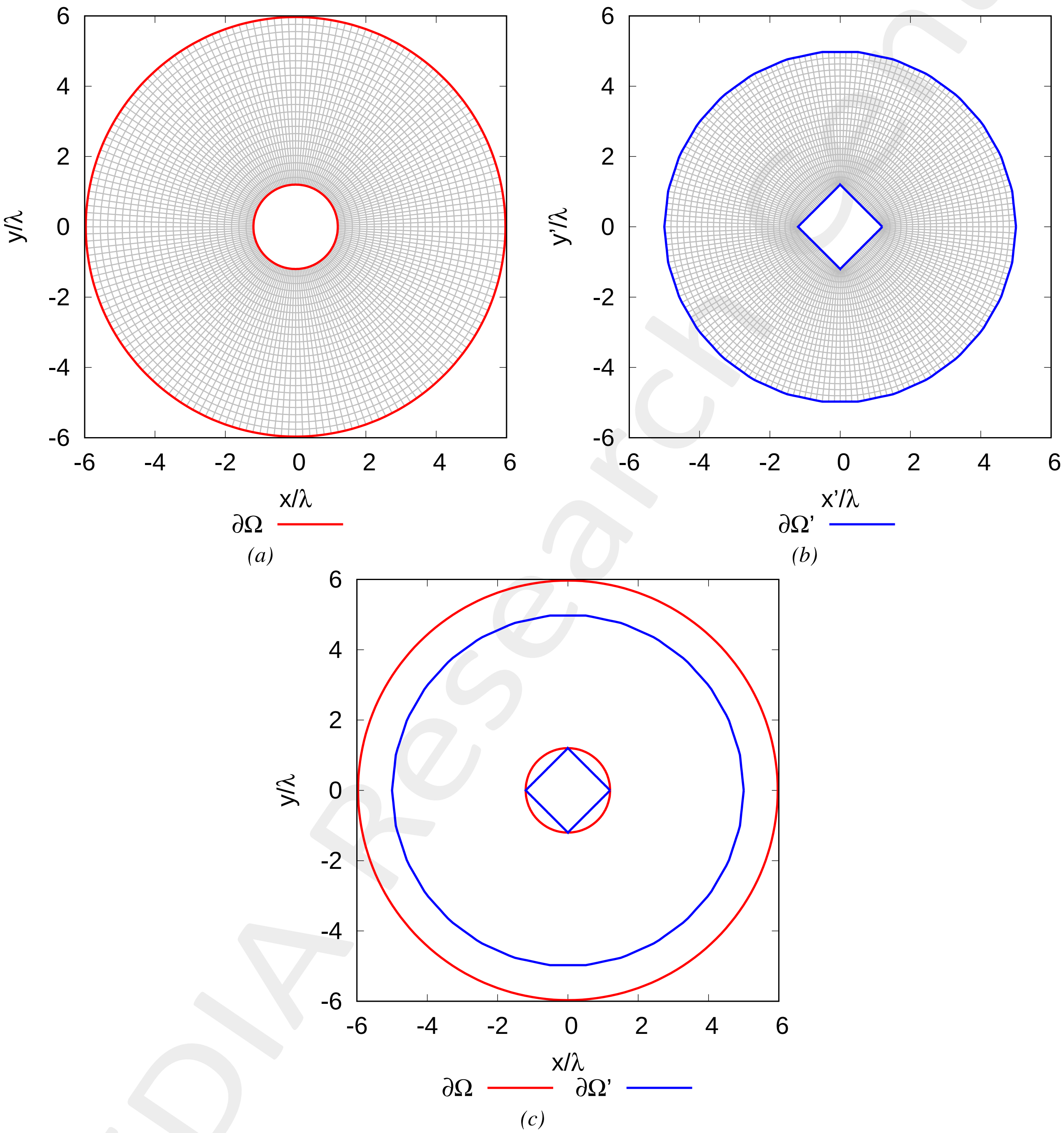

Figure 1: *(a)* Virtual, *(b)* Physical geometries and *(c)* the comparison

- Array:
  - Number of elements: $N = 3, 6$
  - Radius of circular array: $r_{array} = 1.45$ $[\lambda]$
  - Elements spacing: $d = 0.5$ $[\lambda]$

- Schwarz-Cristoffel Transformation:
  - Virtual Region
    - Virtual ground plane radius: $r_{virt-gnd} = 1.2\ [\lambda]$
    - Distance from the ground plane: $\delta = r_{array} - r_{virt-gnd} = \frac{\lambda}{4}$
    - Virtual permittivity: $\varepsilon = 1$
    - Virtual permeability: $\mu = 1$
  - Physical Region
    - External radius: $L_{ext} = 5\ [\lambda]$
    - External Lens boundary : $\partial\Omega_{ext} = \left\{(x, y) \in \mathbb{R} \mid \sqrt{x^2 + y^2} = L_{ext}\right\}\ [\lambda]$
    - Internal Lens boundary: $\partial\Omega_{int} = \{(1.2; 0),\ (0; 1.2);\ (-1.2; 0),\ (0, -1.2)\}\ [\lambda]$
    - Number of points defining the external boundary: $n_{ext} = 30$
    - Number of points defining the internal boundary: $n_{int} = 4$
- SCTO parameters
  - Error tolerance: 10^{-10}
  - Number of Gauss-Jacobi points (nodes): 10
  - Discretization in virtual grid (outer boundary): $\Delta = 0.2\ [\lambda]$
- Simulation Environment
  - Working frequency: $f_w = 300\ [MHz]$
  - Simulation region: $\begin{cases} x \in [-20,\ 20]\ [\lambda] \\ y \in [-20,\ 20]\ [\lambda] \end{cases}$
  - Near-Field computation: $\begin{cases} x \in [-20,\ 20]\ [\lambda] \\ y \in [-20,\ 20]\ [\lambda] \end{cases}$
  - Far-Field computation: $\begin{cases} \theta = \frac{\pi}{2}\ [rad] \\ \varphi \in [0,\ \pi]\ [rad] \end{cases}$
  - Mesh settings
    - Size: $size_{mesh} \in [5 \times 10^{-4}, 0.2]$
    - Maximum growth rate: 1.3
    - Curvature factor: 0.3
    - Narrow region resolution: 1
  - Simulation region layer thickness: 1

2.1.2 Results

Number of elements $N = 3$

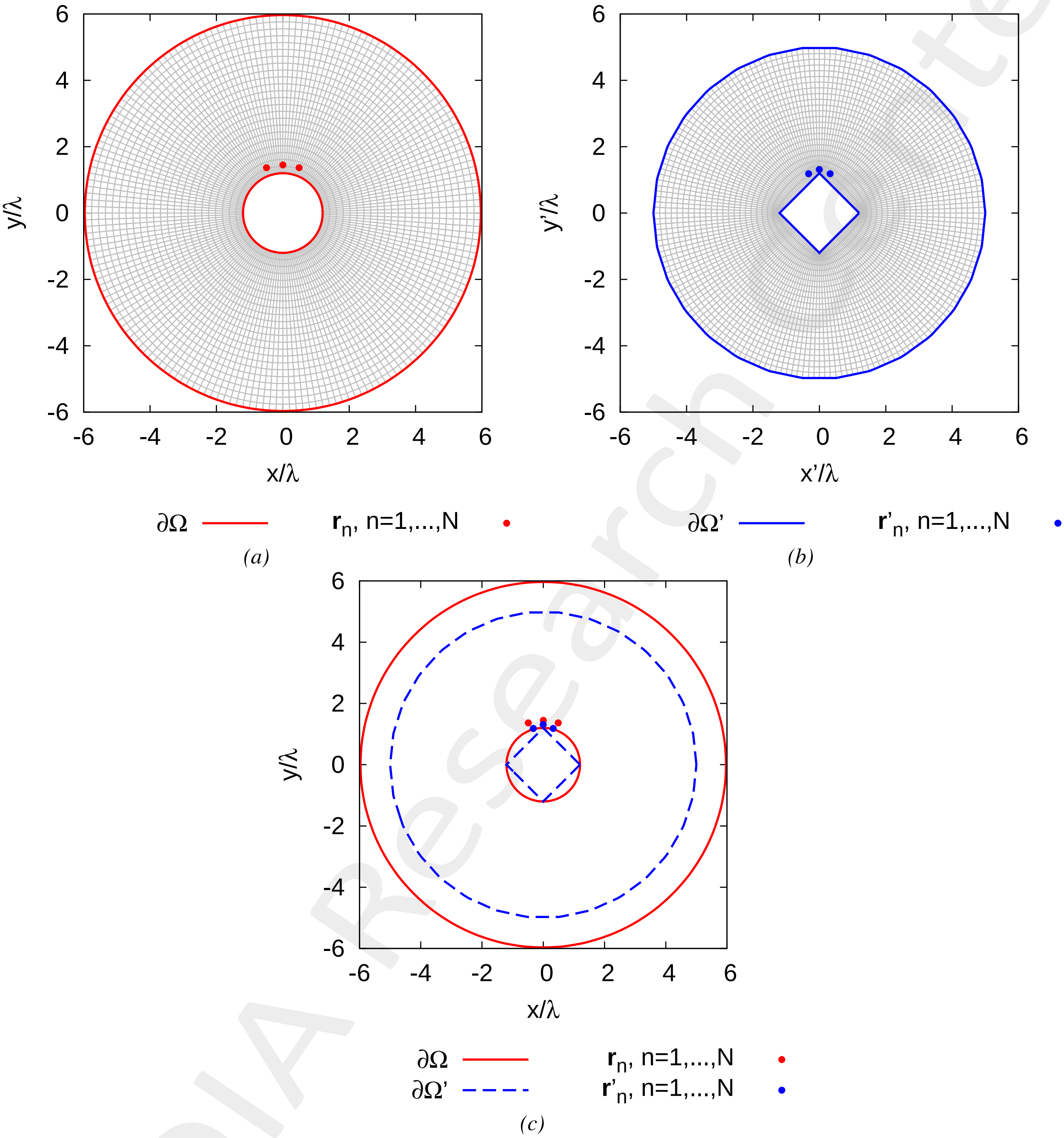

Figure 2: *(a)* Virtual, *(b)* Physical geometries and *(c)* the comparison

Physical Permittivity Properties	
Average fractional anisotropy α_F	0.22161
Average relative anisotropy α_R	0.204644

Table I: Average fractional anisotropy α_F and average relative anisotropy α_R

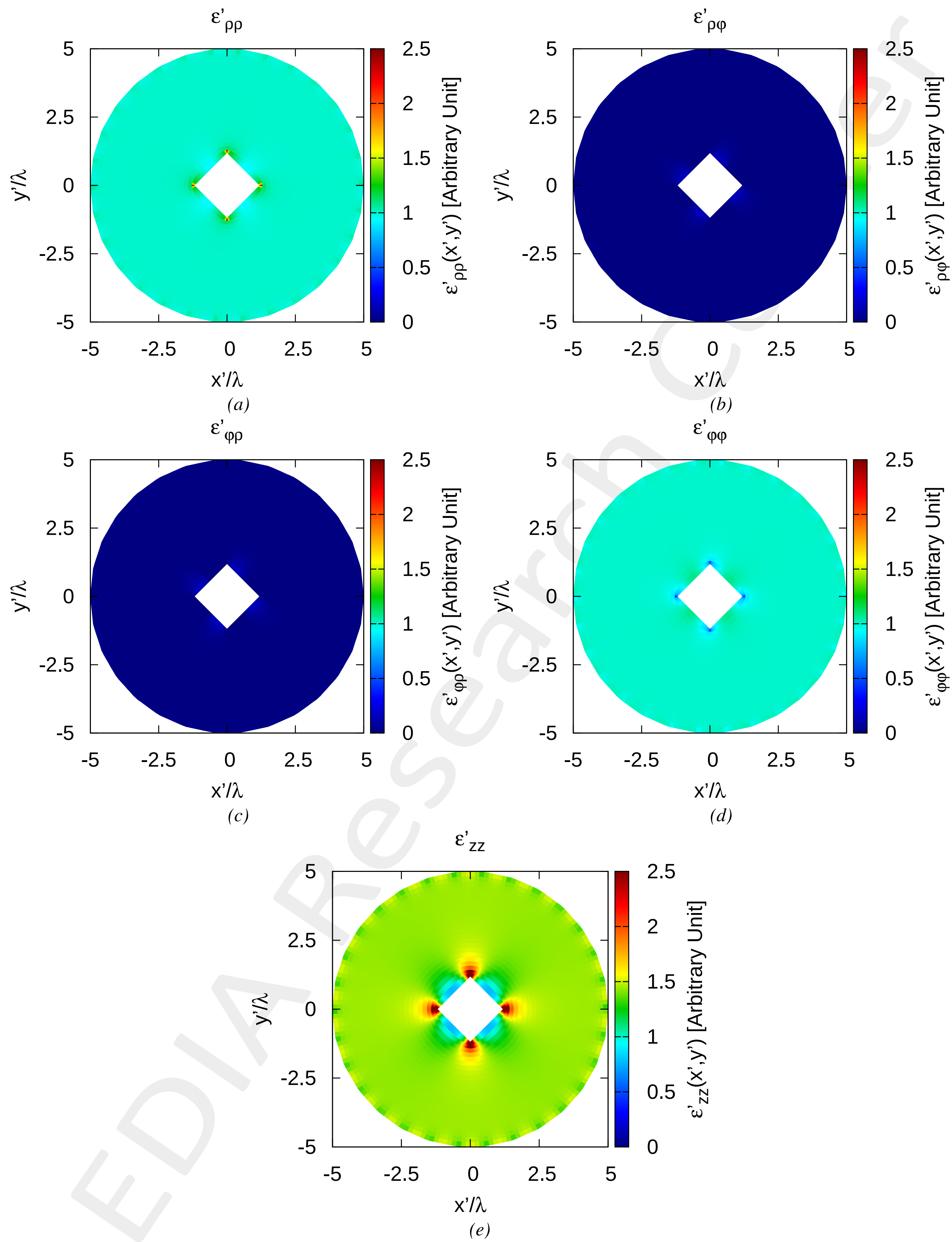

Figure 3: Tensor permittivity values for *(a)* $\varepsilon'_{\rho\rho}$, *(b)* $\varepsilon'_{\rho\varphi}$, *(c)* $\varepsilon'_{\varphi\rho}$, *(d)* $\varepsilon'_{\varphi\varphi}$, *(e)* ε'_{zz}

mimimum/maximum	min	max
$\varepsilon'_{\rho\rho}$	9.2710×10^{-1}	3.1648
$\varepsilon'_{\rho\varphi}$	-3.5262×10^{-1}	1.4413×10^{-1}
$\varepsilon'_{\varphi\rho}$	-3.5262×10^{-1}	1.4413×10^{-1}
$\varepsilon'_{\varphi\varphi}$	3.5526×10^{-1}	1.0789
ε'_{zz}	7.7227×10^{-1}	1.6641×10^{1}
global minimum/maximum	$\min\{\underline{\underline{\varepsilon}}'\} = -0.35$	$\max\{\underline{\underline{\varepsilon}}'\} = 16.64$

Table II: Statistics about the permittivity lens reporting minimum and maximum value for every component of $\underline{\underline{\varepsilon}}'$, global minimum $\min\{\underline{\underline{\varepsilon}}'\}$ and global maximum $\max\{\underline{\underline{\varepsilon}}'\}$

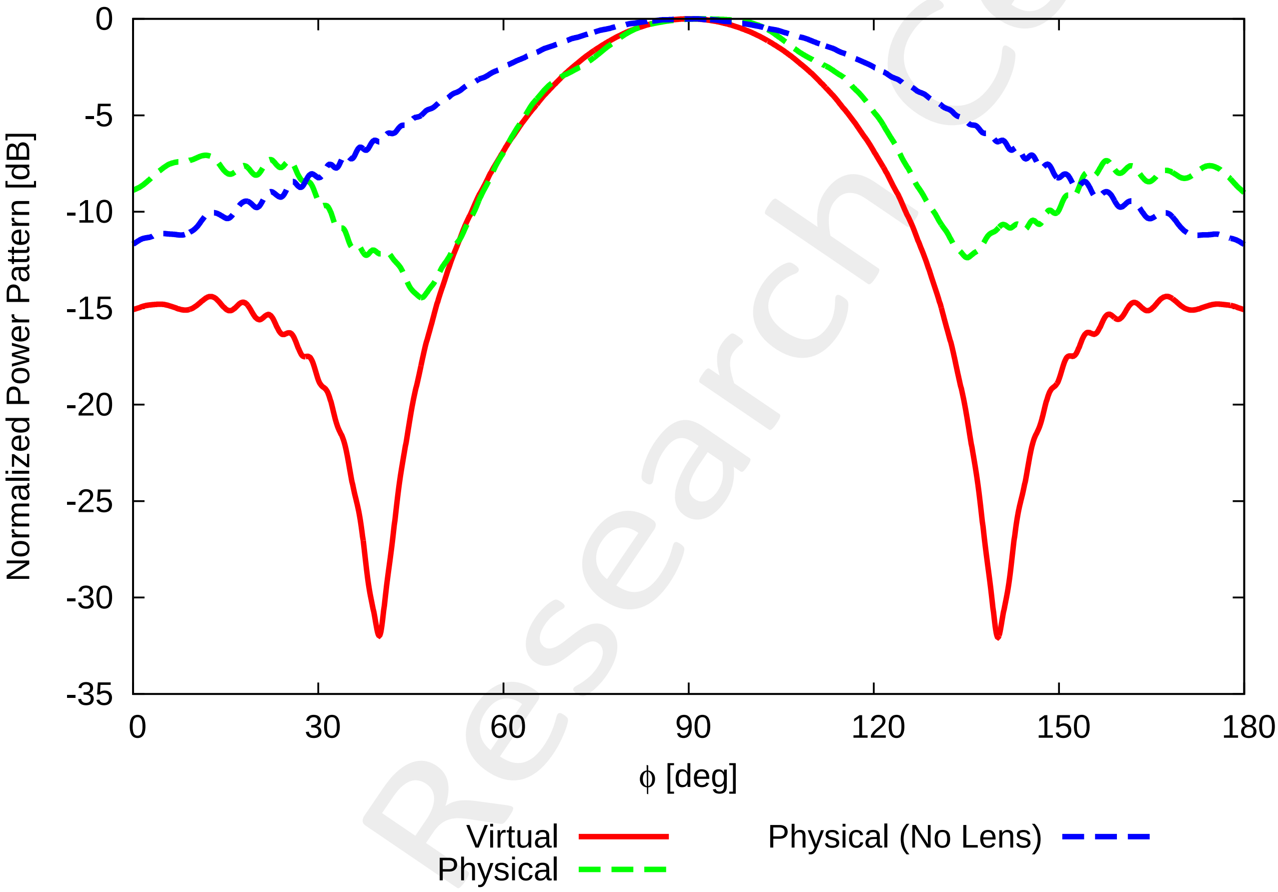

Figure 4: Far-Field Pattern for $\theta = 90$ [deg] and $\varphi \in [0, 180]$ [deg]

	Virtual	Physical	Physical (No Lens)
SLL [dB]	-14.3896	-7.0740	-6.0314×10^{-4}
Directivity [dB]	6.0959	4.9318	3.7901
FNBW [deg]	100.2201	88.4242	47.9039
HPBW [deg]	40.9740	45.5978	65.7429
Field Matching Error ξ (7)	$\times$	8.5441×10^{-2}	1.3728×10^{-1}
Field Matching Error χ (8)	$\times$	2.5214×10^{-1}	7.1538×10^{-1}

Table III: Pattern values for the virtual, physical and physical (no lens) cases

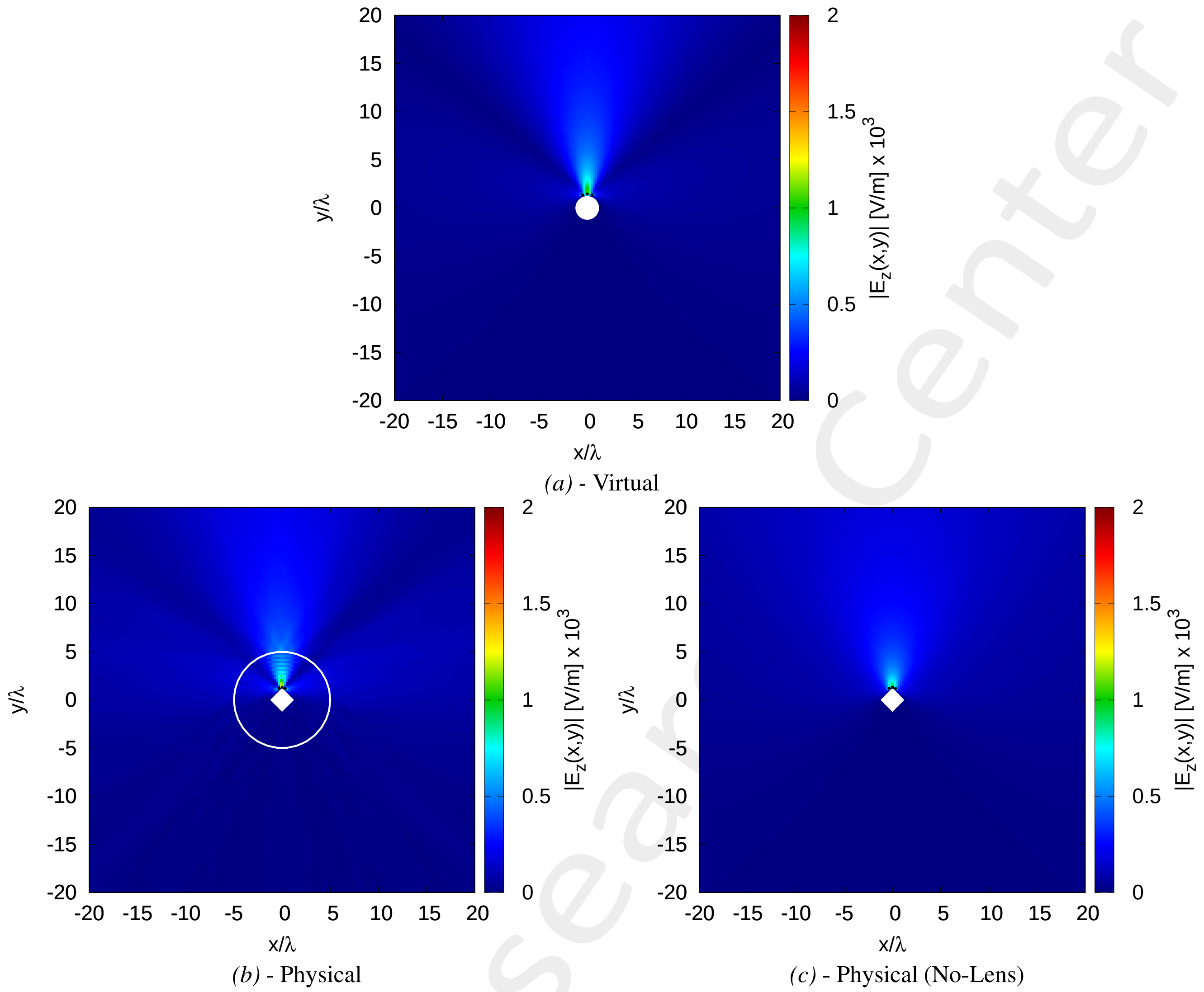

Figure 5: Near-Field pattern in the *(a)* virtual, *(b)* physical and *(c)* no-lens

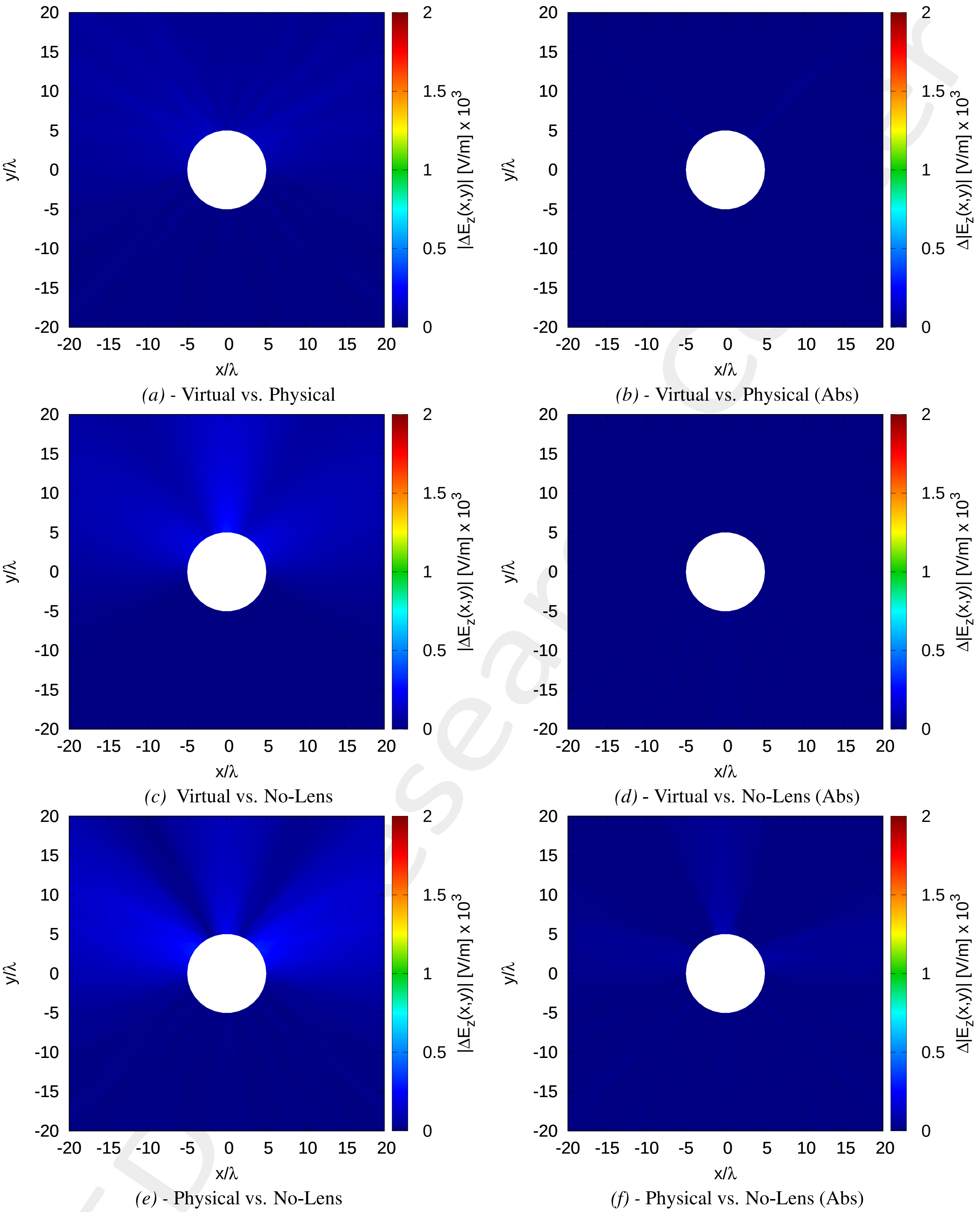

Figure 6: Near-Field difference pattern in the *(a)(b)* virtual vs. physical, *(c)(d)* virtual vs. no-lens and *(e)(f)* physical vs. no-lens. The difference pattern is computed for the *(a)(c)(e)* cases as $|\Delta E_z| \triangleq \left|E_z^{ref}(x,y) - E_z^{est}(x,y)\right|_{(x,y)\notin\Omega}$ while for the *(b)(d)(f)* cases as $\Delta|E_z| \triangleq \left[\left|E_z^{ref}(x,y)\right| - \left|E_z^{est}(x,y)\right|\right]_{(x,y)\notin\Omega}$

Number of elements $N = 6$

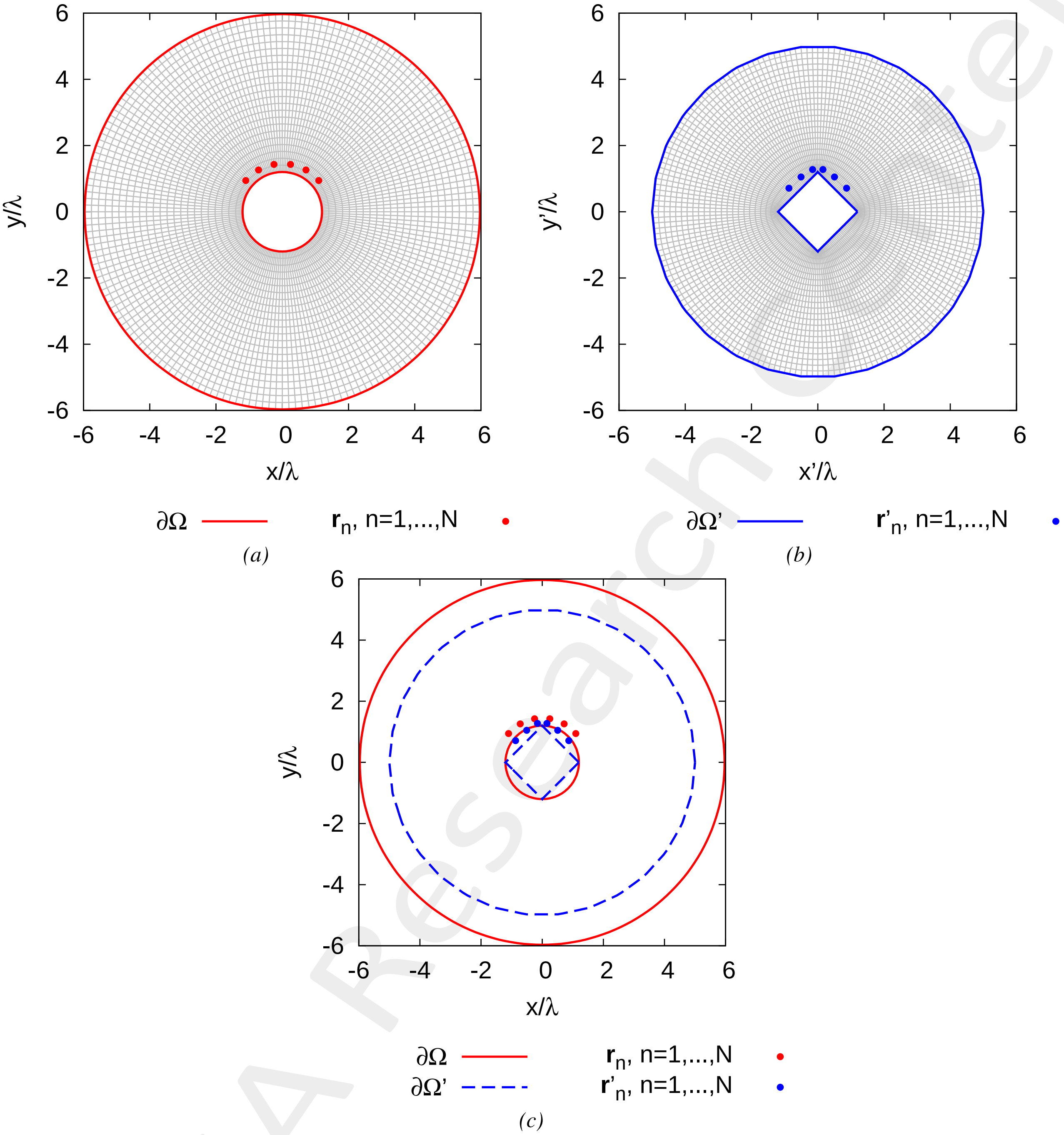

Figure 7: *(a)* Virtual, *(b)* Physical geometries and *(c)* the comparison

Physical Permittivity Properties	
Average fractional anisotropy α_F	0.22161
Average relative anisotropy α_R	0.204644

Table IV: Average fractional anisotropy α_F and average relative anisotropy α_R

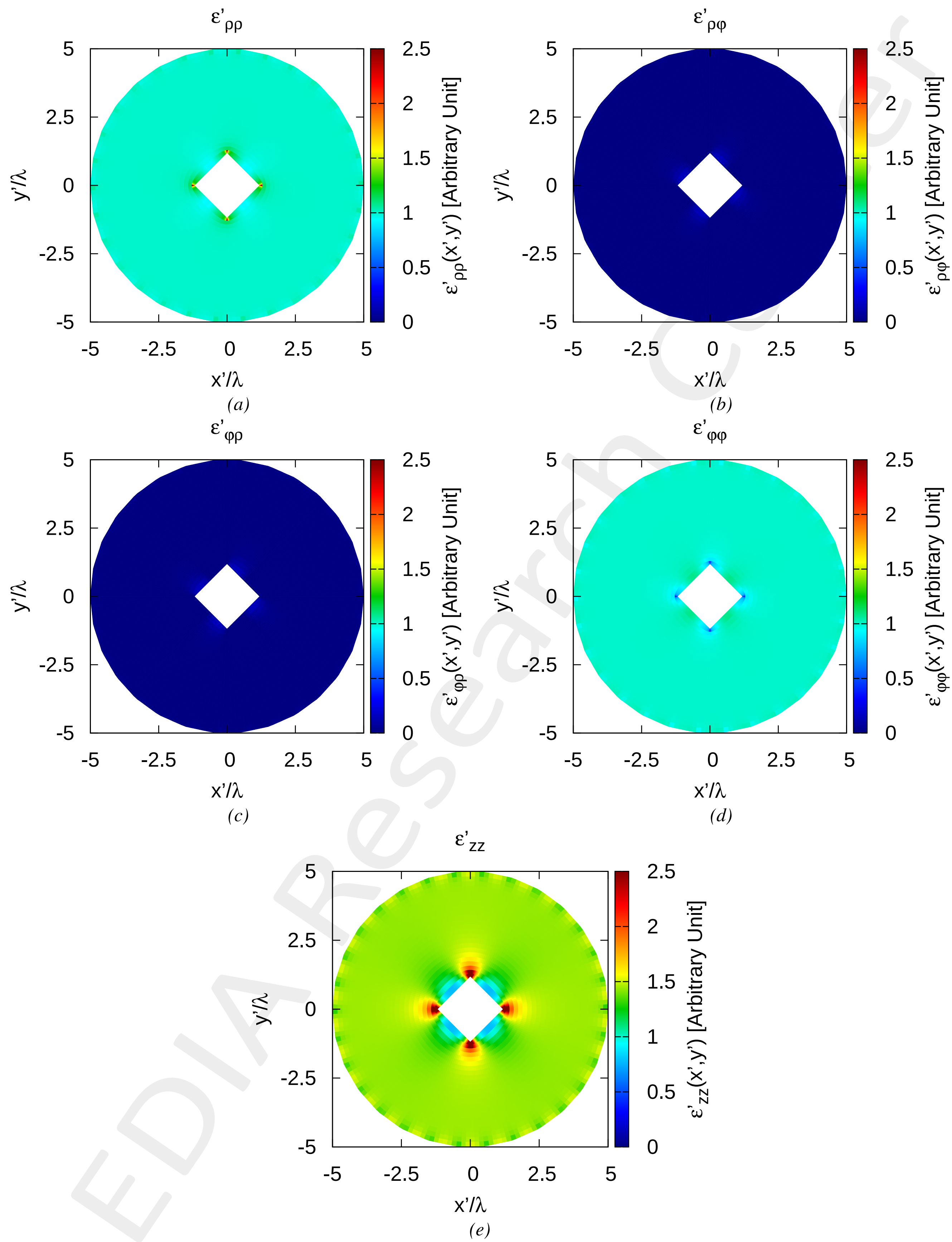

Figure 8: Tensor permittivity values for *(a)* $\varepsilon'_{\rho\rho}$, *(b)* $\varepsilon'_{\rho\varphi}$, *(c)* $\varepsilon'_{\varphi\rho}$, *(d)* $\varepsilon'_{\varphi\varphi}$, *(e)* ε'_{zz}

mimimum/maximum	min	max
$\varepsilon'_{\rho\rho}$	9.2710×10^{-1}	3.1648
$\varepsilon'_{\rho\varphi}$	-3.5262×10^{-1}	1.4413×10^{-1}
$\varepsilon'_{\varphi\rho}$	-3.5262×10^{-1}	1.4413×10^{-1}
$\varepsilon'_{\varphi\varphi}$	3.5526×10^{-1}	1.0789
ε'_{zz}	7.7227×10^{-1}	1.6641×10^{1}
global minimum/maximum	$\min\{\underline{\underline{\varepsilon}}'\} = -0.35$	$\max\{\underline{\underline{\varepsilon}}'\} = 16.64$

Table V: Statistics about the permittivity lens reporting minimum and maximum value for every component of $\underline{\underline{\varepsilon}}'$, global minimum $\min\{\underline{\underline{\varepsilon}}'\}$ and global maximum $\max\{\underline{\underline{\varepsilon}}'\}$

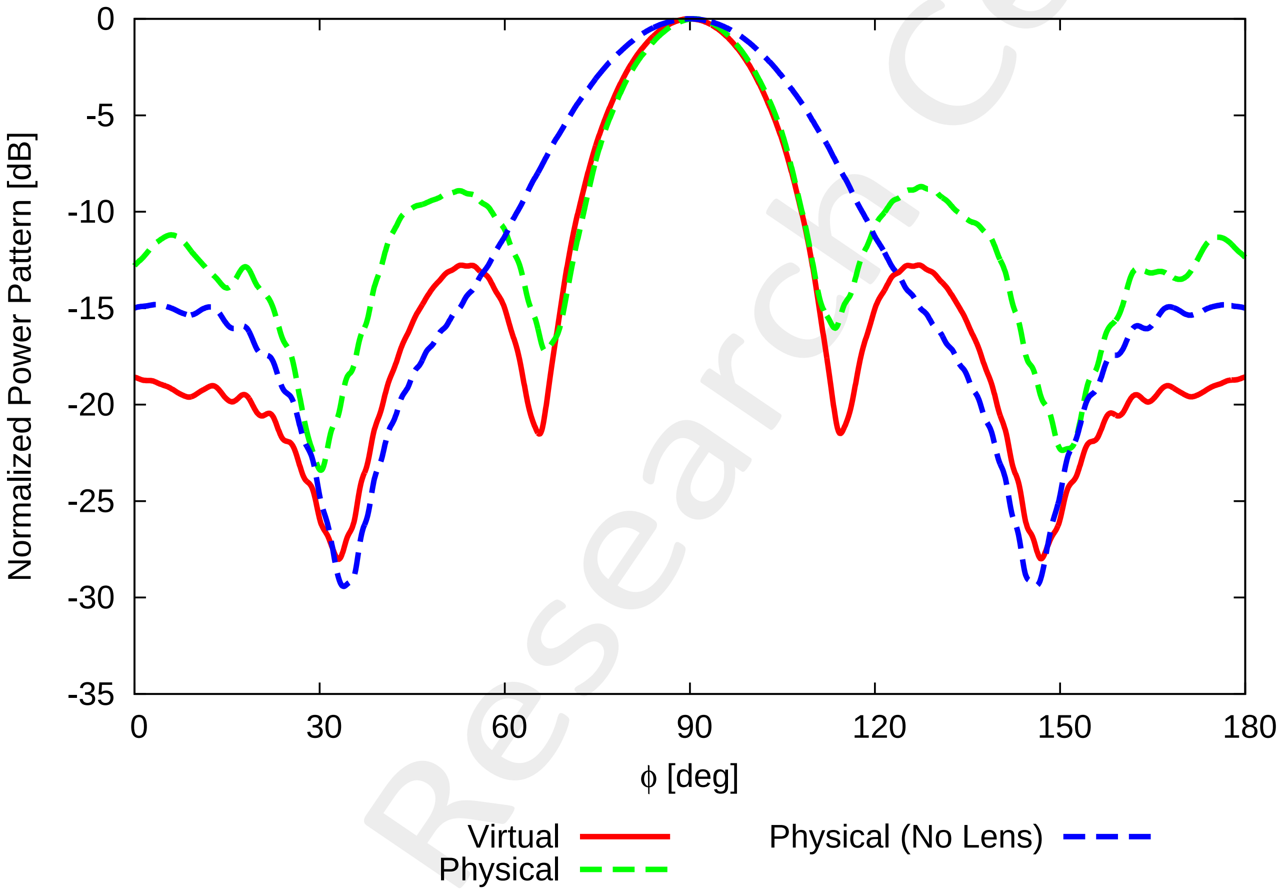

Figure 9: Far-Field Pattern for $\theta = 90$ [deg] and $\varphi \in [0, 180]$ [deg]

	Virtual	Physical	Physical (No Lens)
SLL [dB]	-12.7661	-8.6991	-14.8139
Directivity [dB]	8.7011	7.8727	7.2232
FNBW [deg]	48.7143	46.9134	112.2861
HPBW [deg]	21.3416	20.9393	29.9814
Field Matching Error ξ (7)	$\times$	5.6240×10^{-2}	7.7979×10^{-2}
Field Matching Error χ (8)	$\times$	1.3436×10^{-1}	1.1119

Table VI: Pattern values for the virtual, physical and physical (no lens) cases

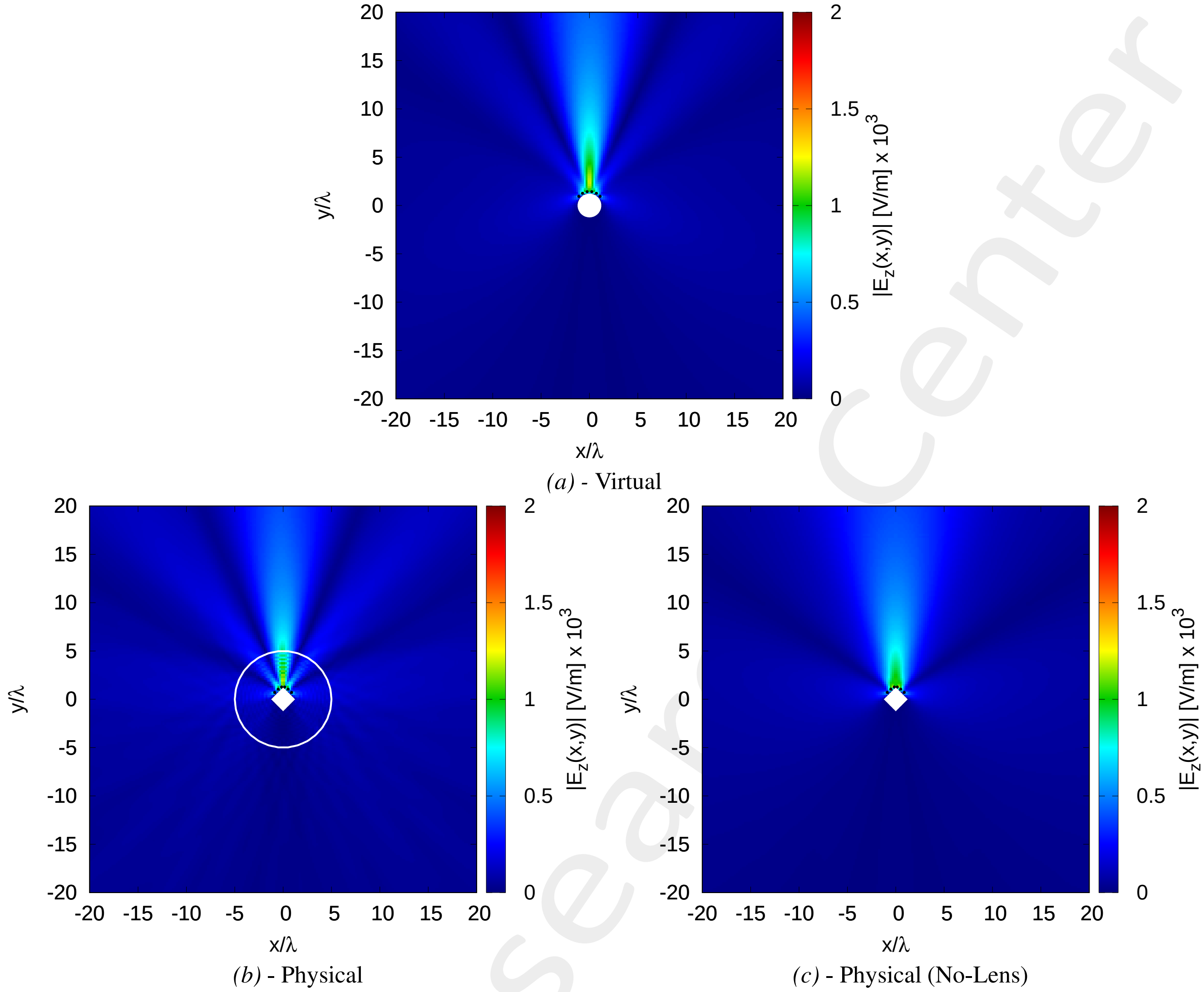

Figure 10: Near-Field pattern in the *(a)* virtual, *(b)* physical and *(c)* no-lens

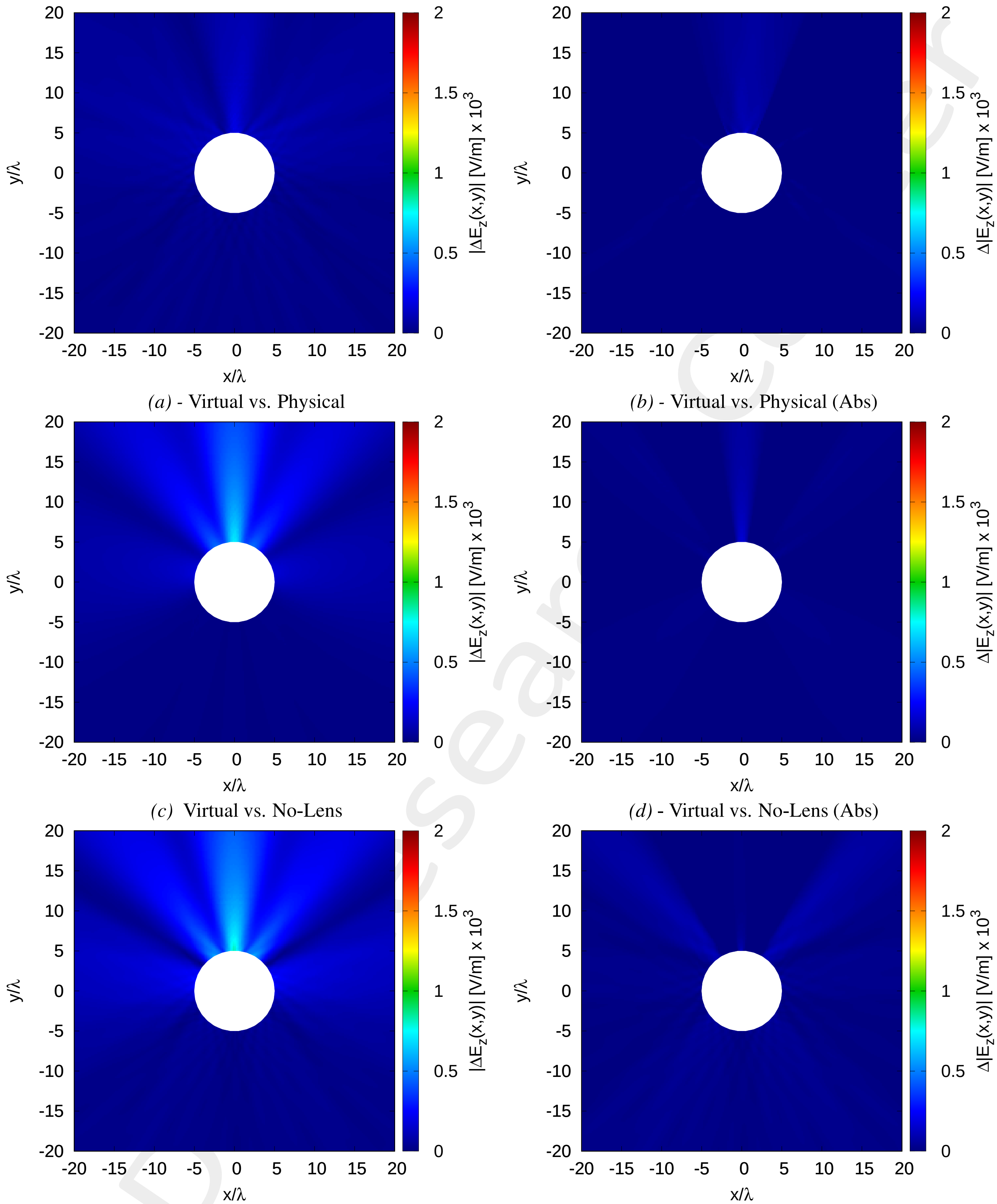

(a) - Virtual vs. Physical

(b) - Virtual vs. Physical (Abs)

(c) Virtual vs. No-Lens

(d) - Virtual vs. No-Lens (Abs)

(e) - Physical vs. No-Lens

(f) - Physical vs. No-Lens (Abs)

Figure 11: Near-Field difference pattern in the *(a)(b)* virtual vs. physical, *(c)(d)* virtual vs. no-lens and *(e)(f)* physical vs. no-lens. The difference pattern is computed for the *(a)(c)(e)* cases as $|\Delta E_z| \triangleq \left|E_z^{ref}(x,y) - E_z^{est}(x,y)\right|_{(x,y)\notin\Omega}$ while for the *(b)(d)(f)* cases as $\Delta|E_z| \triangleq \left[\left|E_z^{ref}(x,y)\right| - \left|E_z^{est}(x,y)\right|\right]_{(x,y)\notin\Omega}$

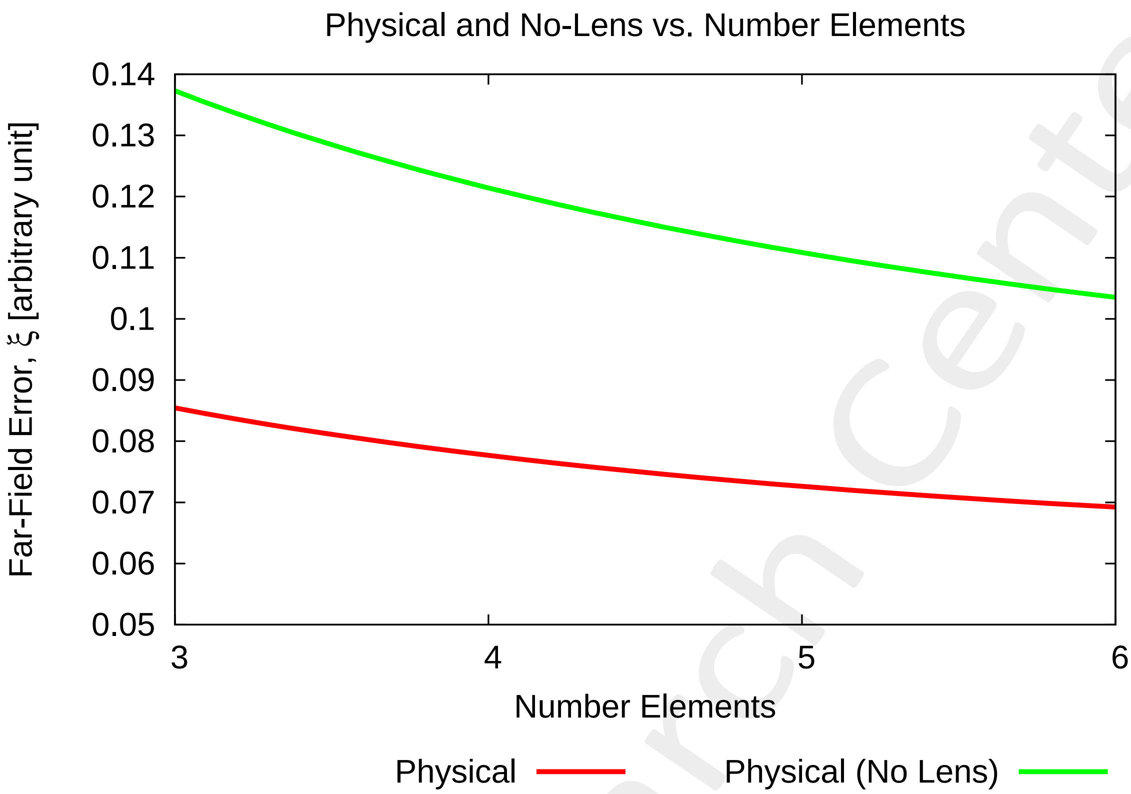

(a)

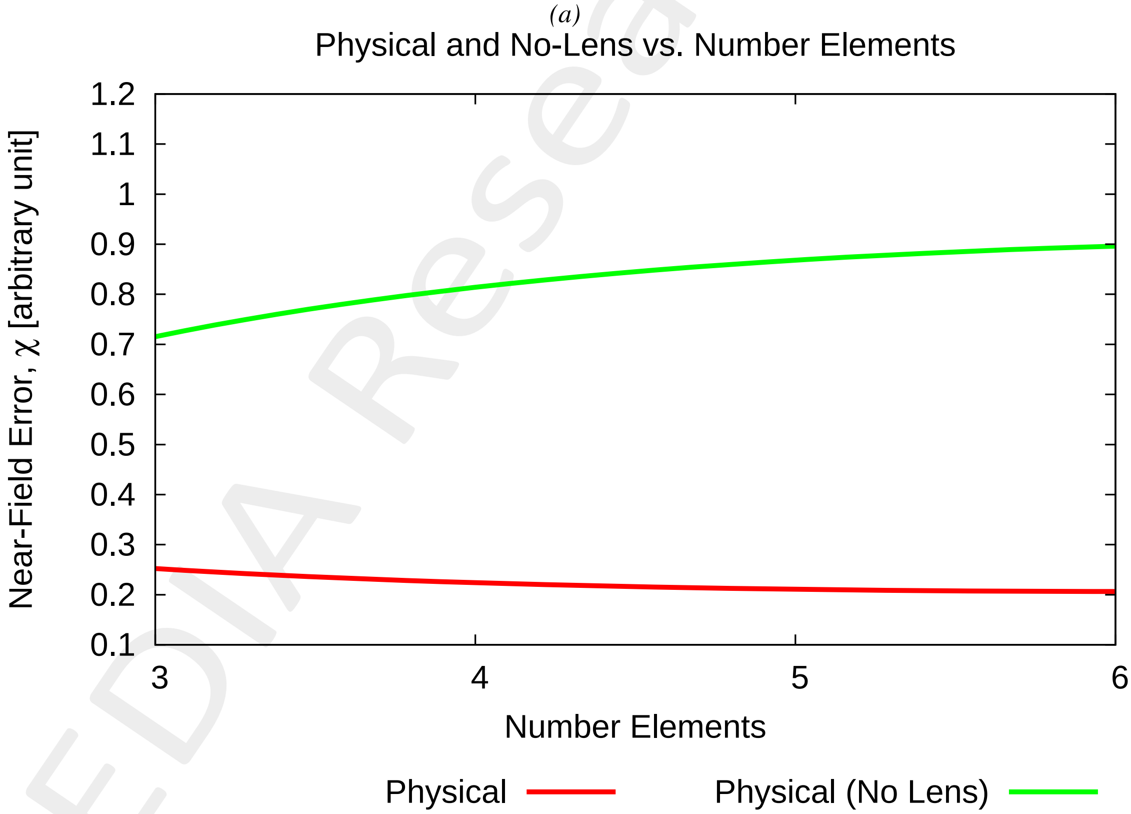

(b)

Figure 12: *(a)* Far-field error ξ and *(b)* near-field error χ for the physical and no-lens cases vs. the number elements

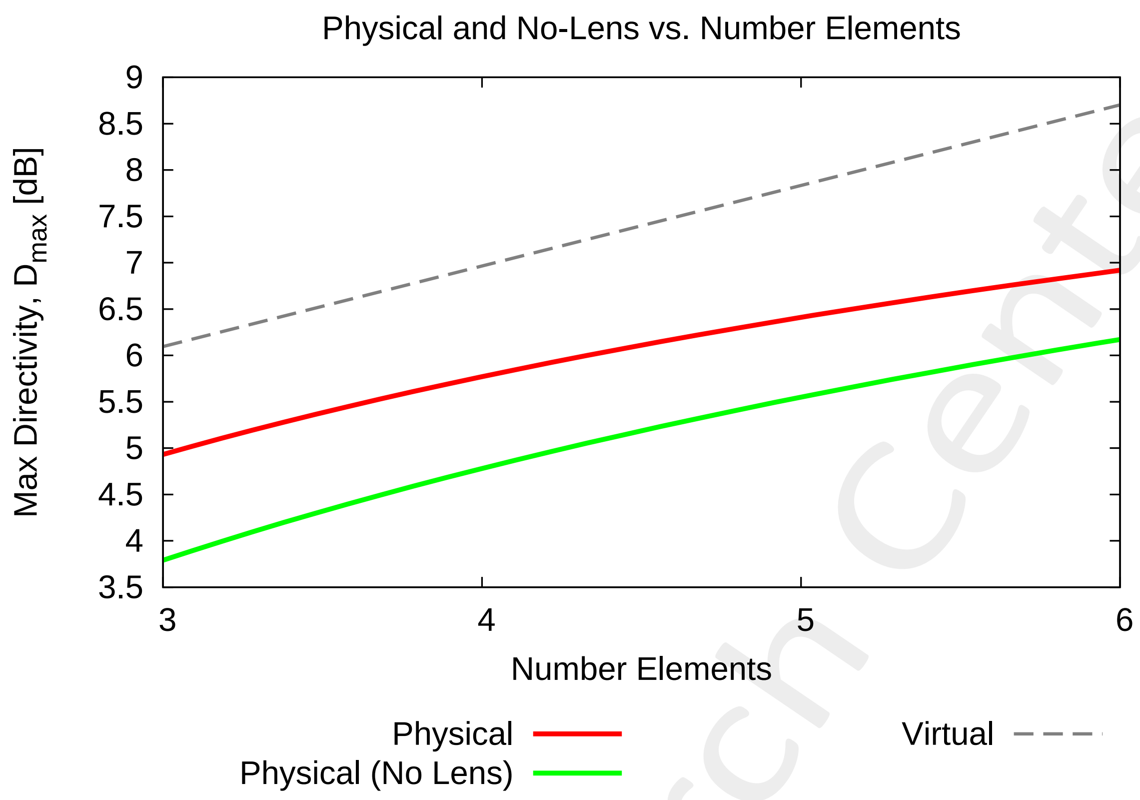

(a)

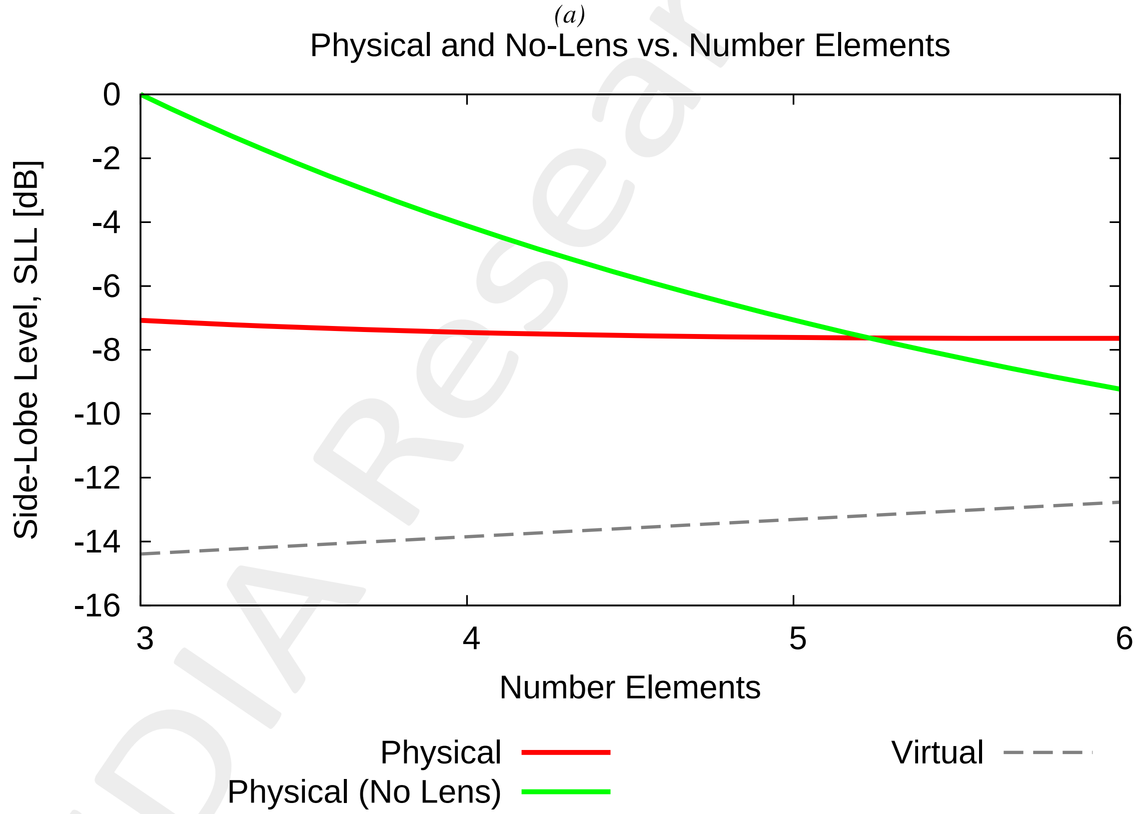

(b)

Figure 13: *(a)* Maximum directivity [dB] and *(b)* sidelobe level (SLL) [dB] vs. the number elements

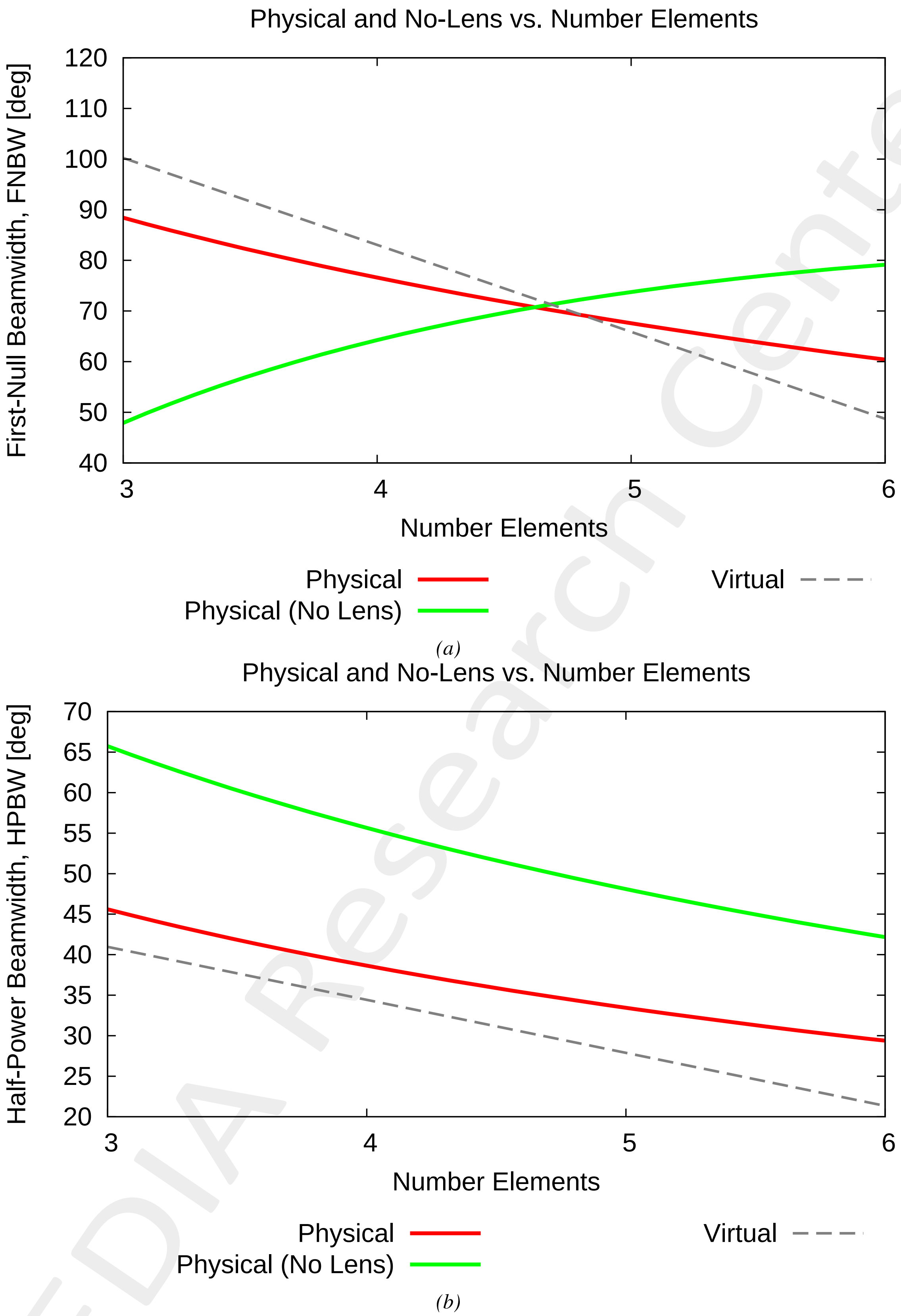

Figure 14: *(a)* First-null beamwidth (FNBW) [deg] and *(b)* half-power beamwidth (HPBW) [deg] vs. the number elements

3 Conclusions

An innovative transformation electromagnetics methodology based on the Schwarz-Christoffel theory has been proposed to design conformal phased arrays. The numerical results have shown the effectiveness and the potential of the proposed method.

References

[1] M. Salucci, F. Boulos, A. Polo, and G. Oliveri, “Conformal transformation electromagnetics based on Schwarz-Christoffel mapping for the synthesis of doubly-connected metalenses,” *IEEE Trans. Antennas Propag.*, vol. 68, no. 3, pp. 1836-1850, Mar. 2020.

[2] M. Salucci, L. Tenuti, G. Gottardi, A. Hannan, and A. Massa, "System-by-design method for efficient linear array miniaturisation through low-complexity isotropic lenses" *Electronic Letters*, vol. 55, no. 8, pp. 433-434, May 2019.

[3] M. Salucci, G. Oliveri, N. Anselmi, and A. Massa, "Material-by-design synthesis of conformal miniaturized linear phased arrays," *IEEE Access*, vol. 6, pp. 26367-26382, 2018.

[4] M. Salucci, G. Oliveri, N. Anselmi, G. Gottardi, and A. Massa, "Performance enhancement of linear active electronically-scanned arrays by means of MbD-synthesized metalenses," *Journal of Electromagnetic Waves and Applications*, vol. 32, no. 8, pp. 927-955, 2018.

[5] G. Oliveri, M. Salucci, N. Anselmi and A. Massa, "Multiscale System-by-Design synthesis of printed WAIMs for waveguide array enhancement," *IEEE J. Multiscale Multiphysics Computat. Techn.*, vol. 2, pp. 84-96, 2017.

[6] G. Oliveri, F. Viani, N. Anselmi, and A. Massa, "Synthesis of multi-layer WAIM coatings for planar phased arrays within the system-by-design framework," *IEEE Trans. Antennas Propag.*, vol. 63, no. 6, pp. 2482-2496, June 2015.

[7] A. Massa and G. Oliveri, "Metamaterial-by-Design: Theory, methods, and applications to communications and sensing - Editorial," *EPJ Applied Metamaterials*, vol. 3, no. E1, pp. 1-3, 2016.

[8] G. Oliveri, E. T. Bekele, M. Salucci, and A. Massa, "Transformation electromagnetics miniaturization of sectoral and conical horn antennas," *IEEE Trans. Antennas Propag.*, vol. 64, no. 4, pp. 1508-1513, April 2016.

[9] G. Oliveri, E. T. Bekele, M. Salucci, and A. Massa, "Array miniaturization through QCTO-SI metamaterial radomes" *IEEE Trans. Antennas Propag.*, vol. 63, no. 8, pp. 3465-3476, Aug. 2015.

[10] L. Tenuti, M. Salucci, G. Oliveri, P. Rocca, and A. Massa, “Surrogate- assisted optimization of metamaterial devices for advanced antenna Systems,” Proc. 2015 IEEE Symposium Series on Computational Intelligence (IEEE SSCI 2015), Cape Town, South Africa, pp. 1154-1156, Dec. 8-10, 2015.

[11] G. Oliveri, L. Tenuti, M. Salucci, and A. Massa, “Innovative antenna architectures exploiting metamaterials for new generation radars,” 10th European Conference on Antennas and Propagation (EUCAP 2016), Davos, Switzerland, pp. 1-3, April 11-15, 2016.

[12] M. Salucci, G. Oliveri, H. Ahmadi, and A. Massa, "Conformal transformation of linear arrays through QCTO-based design tools," Proc. 2016 IEEE AP-S International Symposium and USNC-URSI Radio Science Meeting, Fajardo, Puerto Rico, pp. 1083- 1084, July 26 - July 1, 2016.

[13] M. Salucci, L. Tenuti, E. Bekele, and G. Oliveri, "Enhancement of linear arrays through MbD metamaterial coatings," Proc. 2016 IEEE AP-S International Symposium and USNC-URSI Radio Science Meeting, Fajardo, Puerto Rico, pp. 1089- 1090, July 26 - July 1, 2016.

[14] P. Rocca, N. Anselmi, A. Polo, and A. Massa, "An irregular two-sizes square tiling method for the design of isophoric phased arrays," *IEEE Trans. Antennas Propag.*, vol. 68, no. 6, pp. 4437-4449, Jun. 2020.

[15] P. Rocca, N. Anselmi, A. Polo, and A. Massa, "Modular design of hexagonal phased arrays through diamond tiles," *IEEE Trans. Antennas Propag.*, vol.68, no. 5, pp. 3598-3612, May 2020.

[16] N. Anselmi, L. Poli, P. Rocca, and A. Massa, "Design of simplified array layouts for preliminary experimental testing and validation of large AESAs," *IEEE Trans. Antennas Propag.*, vol. 66, no. 12, pp. 6906-6920, Dec. 2018.

[17] N. Anselmi, P. Rocca, M. Salucci, and A. Massa, "Contiguous phase-clustering in multibeam-on-receive scanning arrays" *IEEE Trans. Antennas Propag.*, vol. 66, no. 11, pp. 5879-5891, Nov. 2018.

[18] N. Anselmi, P. Rocca, M. Salucci, and A. Massa, "Irregular phased array tiling by means of analytic schemata-driven optimization," *IEEE Trans. Antennas Propag.*, vol. 65, no. 9, pp. 4495-4510, Sept. 2017.

[19] N. Anselmi, P. Rocca, M. Salucci, and A. Massa, "Optimization of excitation tolerances for robust beamforming in linear arrays" *IET Microwaves, Antennas & Propagation*, vol. 10, no. 2, pp. 208-214, 2016.